












Imaging Lunar Craters with the Lucy Long Range Reconnaissance Imager (L'LORRI): A Resolution Test for NASA's Lucy Mission

Stuart J. Robbins¹ , E. Beau Bierhaus², Olivier Barnouin³ , Tod R. Lauer⁴ , John Spencer¹ , Simone Marchi¹ , Harold A. Weaver³ , Stefano Mottola⁵ , Hal Levison¹ , and Neil Dello Russo³ 

¹ Southwest Research Institute, 1050 Walnut Street, Boulder, CO 80302, USA

² Lockheed Martin Space Systems Company, P.O. Box 179, Mail Stop S8100, Denver, CO 80201, USA

³ Johns Hopkins University Applied Physics Laboratory, 11100 Johns Hopkins Road, Laurel, MD 20723, USA

⁴ National Optical Astronomy Observatory, Tucson, AZ 85726, USA

⁵ Institute of Planetary Research, DLR, Rutherfordstr. 2, D-12489 Berlin, Germany

Received 2023 May 31; revised 2023 October 4; accepted 2023 October 6; published 2023 December 8

Abstract

NASA's Lucy mission is designed to better understand the unique population of Trojan asteroids. Trojans were probably captured in Jupiter's L4 and L5 points early in the solar system's evolution and little altered since then. A critical investigation of Lucy is to use its highest-resolution camera, the Lucy Long Range Reconnaissance Imager (L'LORRI), to image Trojans' surfaces to understand their geology and impact crater populations. Through crater statistics, the population of smaller bodies that produced those impacts, relative age differences across the bodies, and other comparative investigations between bodies can be studied. Mapping the crater population to the minimum diameters needed to achieve Lucy's objectives might require image subsampling and deconvolution ("processing") to improve the spatial resolution, a process whereby multiple, slightly offset images are merged to create a single, better-sampled image and deconvolved with L'LORRI's point-spread function. Lucy's first Earth Gravity Assist (EGA1) provided an opportunity to test this process's accuracy using L'LORRI images of the Moon, whose crater population is well characterized and therefore provides ground-truth testing. Specifically, the lunar crater imaging by L'LORRI during EGA1 allowed us to compare crater statistics derived from raw and processed L'LORRI images with ground-truth statistics derived from higher-resolution lunar imaging from other missions. The results indicate the processing can improve impact crater statistics such that features can be identified and measured to $\approx 70\%$ the diameter that they can otherwise be reliably mapped on native L'LORRI images. This test's results will be used in the observation designs for the Lucy flyby targets.

Unified Astronomy Thesaurus concepts: [The Moon \(1692\)](#); [Jupiter trojans \(874\)](#); [Craters \(2282\)](#); [Lunar craters \(949\)](#); [Astronomy image processing \(2306\)](#); [Observational astronomy \(1145\)](#)

1. Introduction

The geology of almost all solid solar system bodies is affected in a large part by impact craters. These craters form as cavities into target surfaces with initial conditions well characterized from decades of observational, laboratory, computer, and theoretical observations. Modifications from expected initial conditions can be used to infer information about unique formation conditions such as target body characteristics and/or how the craters were modified since their formation. Such studies are critical to understanding the properties of the near-surface of solar system bodies and their geologic history.

Additionally, the population of impact craters can be used, in conjunction with applicable scaling laws, to understand the population of impactors that formed the craters. Hypervelocity impact craters always have cavities larger than the impactors that formed them, and so the smallest observable craters can yield information about even smaller, unobservable impactors. Understanding the size–frequency distribution of impactors throughout the solar system is critical for understanding fields as far-ranging as present-day impact hazards at Earth to modeling how the solar system itself formed and dynamically

evolved. Craters on the Trojans can also be used to understand relative ages based on any differences in crater spatial densities, model absolute ages based on dynamic impact models, and other morphologic cross-body investigations.

The Trojan asteroids, co-orbiting the Sun with Jupiter, form a population of bodies that heretofore have been unobserved at ranges close enough to resolve them as geologic bodies. NASA's Lucy mission will be the first to study several Trojans up-close (Levison et al. 2021). Two of the top-level science goals of Lucy include understanding these bodies' crater populations across a wide range of crater diameters (assuming the bodies are cratered; Marchi et al. 2023). Understanding how well images taken with Lucy's highest resolution camera can be used to reproduce a known crater population is critical for understanding potential biases or limitations for imaging unknown crater populations. Additionally, understanding how image subsampling and deconvolution could potentially help to accurately recover craters that are not otherwise resolvable is important for understanding whether even smaller impact craters can be reliably studied.

Toward this goal, Lucy's Long Range Reconnaissance Imager (L'LORRI; Weaver et al. 2023) was used to image Earth's Moon during Earth Gravity Assist 1 (EGA1), described in Section 2. Images taken with L'LORRI were used to identify lunar impact craters, described in Section 3. In Section 4, the methods used to analyze the crater populations are described,



Original content from this work may be used under the terms of the [Creative Commons Attribution 4.0 licence](#). Any further distribution of this work must maintain attribution to the author(s) and the title of the work, journal citation and DOI.

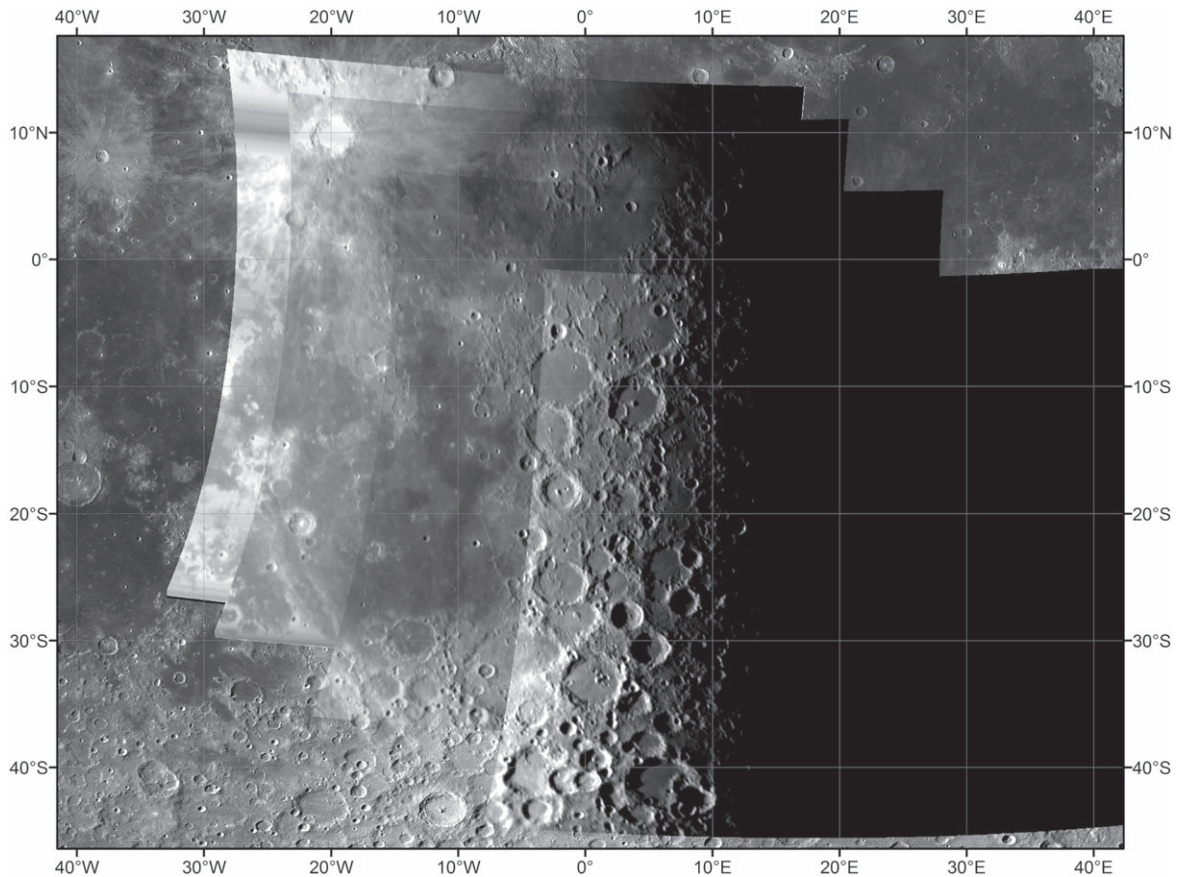


Figure 1. A wide section of the Moon, with the LROC-WAC morphologic mosaic as the basemap. Overlaid are the four different L'LORRI images that were used in this test. Images are not photometrically corrected, so the lunar phase function and topographic shading are readily visible; images were stretched with 0.5% level clips of both the darkest and lightest pixels for this display. The first image in the sequence (upper left) is saturated over the western region, and the second image is saturated over Copernicus crater, since L'LORRI was not designed to image objects as bright as the Moon at 1 au. The lunar terminator was at approximately +10°E during imaging, so only approximately 20% of the final image of the sequence could be used.

and the results are presented in Section 5. Section 6 discusses the implications of this work.

2. Imaging and Image Processing

2.1. Lunar Images Acquired by L'LORRI

Approximately 6 hr after Lucy's closest approach to Earth on 2022 October 16, Lucy was pointed toward the center of the lunar disk and an imaging sequence commenced: 400 images were taken in 10 clusters, which were separated only by small temporal gaps (we refer to each cluster of images as "drift pointings"). Within each cluster of 40 images, 20 images had 2 ms exposure times and 20 images had 5 ms exposure times. The spacecraft remained pointed at a fixed R.A./decl. in space while the Moon moved through it. The first image acquired was centered approximately at lunar coordinates (-5°N , -5°E), and the final was acquired with center coordinates at approximately (-30°N , $+30^{\circ}\text{E}$). The lunar terminator at the time of imaging was at approximately $+10^{\circ}\text{E}$, so large parts of later images in the sequence were in shadow (Figure 1).

The nominal ground pixel scale of the images is approximately 1.25 km pix^{-1} , and the $1024 \times 1024 \text{ pix}$ detector produced images that span approximately $45^{\circ} \times 45^{\circ}$ across the Moon. The camera's field of view, in conjunction with the pointing geometry, means the images covered solar incidence angles $i \gtrsim 50^{\circ}$, with areas near $i \sim 50^{\circ}$ and $i \sim 90^{\circ}$ unsuitable for robust crater detection due to how short or long the shadows

cast by craters are (Wilcox et al. 2005; Ostrach et al. 2011; Richardson et al. 2022).

2.2. Selected Lunar Images for Analysis

For this test, we selected one representative image from the first, second, fourth, and seventh drift pointings. While the eighth, ninth, and tenth captured some area to the southeast that were not in the seventh, it was fairly little terrain by area and would not affect the overall test, so they were omitted. Specifically, the following L'LORRI images were used: lor_0719213468_02520, lor_0719213573_02522, lor_0719213783_02526, and lor_0719214099_02532. The longer string of numbers in each corresponds to the mission-elapsed time (MET), indicating approximately 10.5 minutes elapsed between the first and last image used, so the illumination and geometric considerations are practically identical throughout the sequence; this was verified by not observing any noticeable differences from image to image (i.e., incidence angle, emission angle, phase angle, pixel scale).

2.3. Producing a Subsampled and Point-spread-function-deconvolved Image Stack

Deconvolution is most effective when the image and point-spread function (PSF) are at least Nyquist sampled. With a measured size of about 2.7 native L'LORRI pixels' FWHM (Weaver et al. 2023; Figure 2), the L'LORRI PSF is marginally Nyquist sampled. The first step of our process was to combine

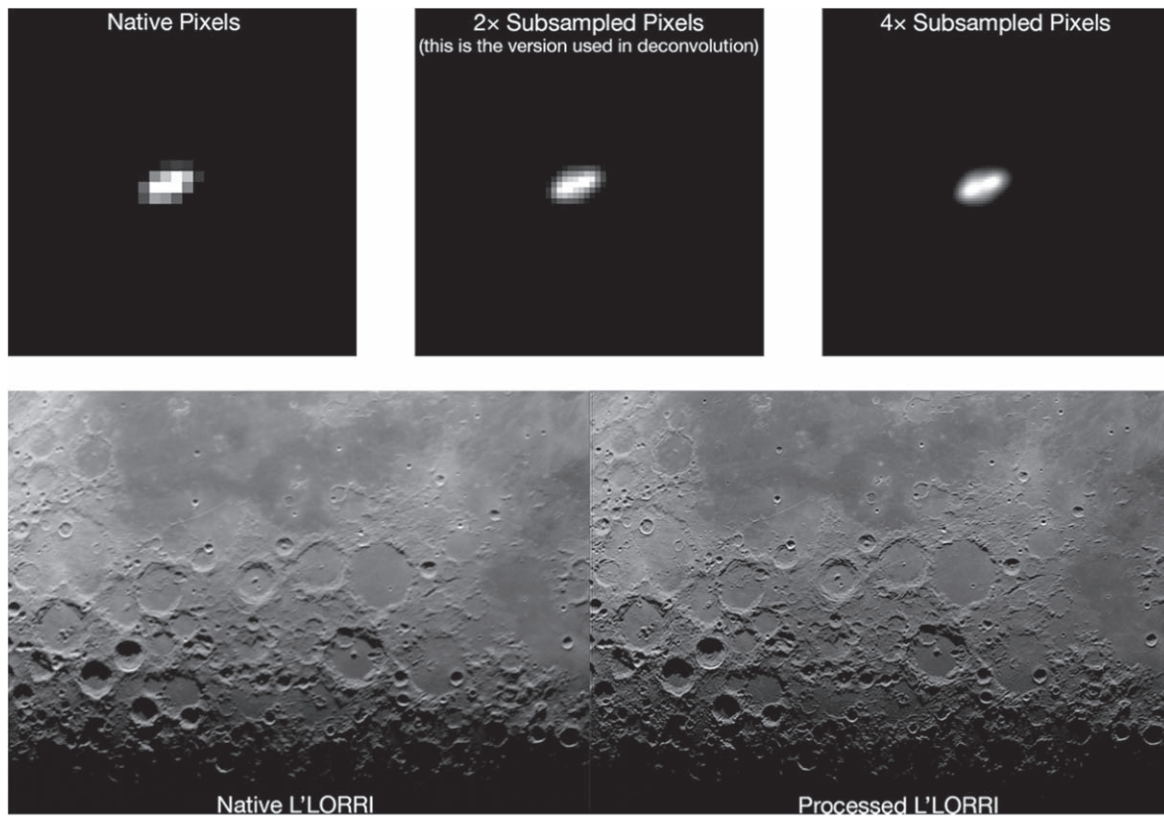


Figure 2. Shortly after the main lunar observations were taken, the L’ORRI boresight was offset from the Moon to capture images of a nearby star field, from which we constructed a well-sampled PSF that could be used to deconvolve the L’ORRI lunar images. This PSF is displayed here, in the top row, in three different formats: with native pixels, with double-sampled pixels as was used in the deconvolution (“2×”), and with quadruple-sampled pixels (“4×”). Each image is centered on the pixel with maximum intensity, is displayed on a linear scale from 0 to the maximum value, and covers the same physical area on the CCD (adapted from Weaver et al. 2023). The bottom row shows one image from one of the drift pointings and the processed L’ORRI image made from a combination of it and other images taken in the same cluster.

several dithered images, which was done for Weaver et al. (2023), to increase our understanding of the PSF to the half-pixel level (~ 5.4 subsampled pixels’ FWHM). This improved knowledge of the PSF improves the effectiveness of the deconvolution we will apply to the images.

With the PSF subsampled by 2, we must similarly subsample the images. However, we did not deconvolve any single image, but an aligned, subsampled stack of source images. Therefore, our second step was to subsample images we would use, by a factor of 2, and our third step was to align and stack those subsampled images. Purposely dithered images by exactly one-half pixel can simply be interlaced to generate a well-sampled image. Since purposeful dithering was not done in this imaging test, image combination was done with the Fourier-based algorithm of Lauer (1999). This method effectively interlaces a set of potentially nonoptimally dithered images to generate a summed image with a finer pixel scale without introducing additional blurring. Aligning the images is accomplished by measuring relative offsets within each image based on the centroids of bright, compact features, so it does not require any a priori knowledge of pointing or any minimum pointing stability.

The fourth step was to perform the deconvolution. Deconvolution can amplify random noise, and it can introduce artifacts (typically ringing at the edges of sharp, high-amplitude features in the image) that can be confused with real source structure. Specifically, for our purposes, such ringing can bear a striking resemblance to poorly resolved impact craters. However, deconvolution has been increasingly recognized

(based on increasing citation rates and usage) as a valuable research tool in astronomy since the advent of digital imagers with well-understood responses: When correctly applied, deconvolution can recover real structural information in an image that can be exceedingly difficult to access by other methodologies. For example, researchers on the Deep Impact mission successfully implemented deconvolution to recover real structure at comet Hartley 2 after a flaw in prelaunch calibration led to an inability to accurately focus the spacecraft’s high-resolution instrument (e.g., Lindler et al. 2013). In our lunar test, deconvolution of the well-sampled L’ORRI image stack was done with the Lucy–Richardson algorithm (Richardson 1972; Lucy 1974), which has a strong heritage of use with optical imagers. It was also used heavily in the preparation of New Horizons LORRI images (Schenk et al. 2018a, 2018b), including the study of Charon’s impact craters (Robbins et al. 2017).

In summary, the overall method presented in Lauer (1999) was used to produce what we refer to as “processed” images for the remainder of this work, in contrast with “native” images. Their process begins by creating a subsampled PSF, and then subsampling and stacking native L’ORRI images so a single stack is subsampled the same way as the PSF. The stack is then deconvolved with the L’ORRI PSF. For this work, that process was performed for each batch of 10 drift pointings using 16 images in the stacking process for each drift pointing. The drift pointings we used correspond to the first, second,

fourth, and seventh drift pointings to directly compare against craters mapped on the native L’LORRI images.

From this process, one might assume that the effects of L’LORRI’s elongated PSF could be removed. If the PSF were not as severe as it is, this assumption might be true. However, the significantly elongated nature of the PSF effectively results in zeros that cannot be recovered: There are values of 0 in the Fourier domain, which are zones where the power at distinct spatial frequencies is nulled out. This represents a loss of information because of the PSF, and that loss cannot be recovered by any deconvolution algorithm of which we know. Ergo, even in the deconvolved images, the elongated PSF is readily apparent in its effects on small features.

2.4. Seleno-rectification

ESRI’s ArcMap software, common in planetary geologic mapping, can take a raster image and through the use of manual control points warp the image to a cartographic system, exporting the result with embedded geographic data (e.g., a GeoTIFF file). ArcMap was used on the native and processed L’LORRI images. Approximately 60 control points were manually created for each image, and a third-order polynomial was fit to the distribution. The control points were made using to the Lunar Reconnaissance Orbiter Camera’s Wide-Angle Camera (LROC-WAC) 100 m pix^{-1} basemap as the coordinate system (Robinson et al. 2010). Care was taken along the image edges and corners, or the terminator when edges or corners were in lunar night. The rectification was done independently for each image using bicubic interpolation, and the final results for each image agreed with others to within approximately 1 L’LORRI pixel. While this will produce some blurring as any map projection would, visual inspection of corners of one image relative to the interior of another showed no obvious blurring effects.

3. Crater Identification and Post-hoc Selection

3.1. Regions of Interest

Regions of each of the four main images were masked to eliminate saturation and solar incidence that was either too high or too low. A consistent cutoff between -25.2° and $+8.7^\circ$ E was used to bracket the regions of interest; this longitude range corresponds approximately to incidence angles between 55° and 89° .

3.2. Crater Identification and Measurement

The first author (S.J.R.) performed the majority of the crater identification and measurement, analyzing all images noted in the previous section (Figure 1). To blind the data gathering to try to eliminate remembering the scene from one image to the next, to the extent practical for this exercise, we did not identify craters on more than one image per day. Additionally, any craters previously identified were hidden so that identifications could be as independent as possible. Features were identified to small sizes independent of an a priori minimum pixel diameter, where the criterion was simply that the analyst be reasonably confident the feature is a real impact crater. Craters identified by an analyst on multiple images with overlapping regions were combined so that there were two data sets per analyst to study: craters from native images, and craters from processed images.

S.J.R.’s method of crater measurement is to trace the rims in ArcMap software. In other analysis software, both circles and ellipses are fit to the rim traces. Multiple, unconstrained circle-fitting algorithms are used, and the result that agrees best among the different methods and with the ellipse fit is saved. Ellipses are fit to the rim traces using a maximum-likelihood approach (Szpak et al. 2015). Robbins (2019) goes into significantly more detail about the fitting process.

4. Analysis Methods

The analysis was done using two primary methods. The first was to use the standard technique of a size–frequency distribution (SFD), using both the cumulative (CSFD) and relative (RSFD) display methods. Specifically, the SFD_{EDF} method described in Robbins et al. (2018) was used; the Appendix illustrates agreement with more classic binned methods. SFD_{EDF} represents each impact crater diameter as a probability distribution (e.g., a Gaussian, with a mean diameter at the measured diameter and a Gaussian width based on repeatability experiments) and sums those probability distributions to yield a final empirical distribution function (SFD_{EDF}). This probability distribution is in contrast with classic methods that represent an impact crater as having a single, specific diameter (which is, itself, the δ function probability distribution). SFD_{EDF} calculates uncertainty envelopes using a bootstrap-with-replacement algorithm that takes into account the entire data set rather than just uncertainties at any given diameter bin, so the uncertainties are not comparable between this and the classic $N^{1/2}$ Poisson uncertainties. In the limit of the probability distribution for each crater being a δ function, $\text{SFD} = \text{SFD}_{\text{EDF}}$.

SFD_{EDFs} were constructed for crater populations observed within the mapping described in Section 2.2. The SFD_{EDFs} were then compared against the existing Robbins (2019) impact crater database that was augmented with confidence measurements for each crater. That database is complete for craters ≈ 1 –2 km and larger, and it has generally stood up to scrutiny, especially for larger impacts. It is those larger impacts ($\gtrsim 5$ km) that are needed here since, with a native L’LORRI pixel scale of 1.25 km, even on the processed images we would not expect to identify a complete sampling of craters smaller than ~ 5 km (4 native pixels).

The second analysis method was to examine each individual crater identification and compare with the Robbins (2019) database. The purpose was to quantify true positives (TPs), false positives (FPs), and false negatives (FNs); that is, real craters positively identified, not-craters that were identified as craters, and real craters that were not identified. One purpose of this analysis was to determine if the SFD analysis produced the correct SFD shape (relative to ground truth) because it allowed identification and measurement of smaller craters, or if it brought out false features that happened to follow a familiar SFD. This crater–crater comparison also allows a direct comparison of crater diameters to determine if there is any broadening effect to larger diameters.

To conduct this second analysis, features identified on the L’LORRI images must be matched to those in the Robbins (2019) database. To match, a modified DBSCAN cluster analysis was run (Ester et al. 1996; Robbins et al. 2014). DBSCAN has a primary cluster variable called a “reachability parameter,” where one feature must be close enough to another feature to be considered members of the same cluster. The

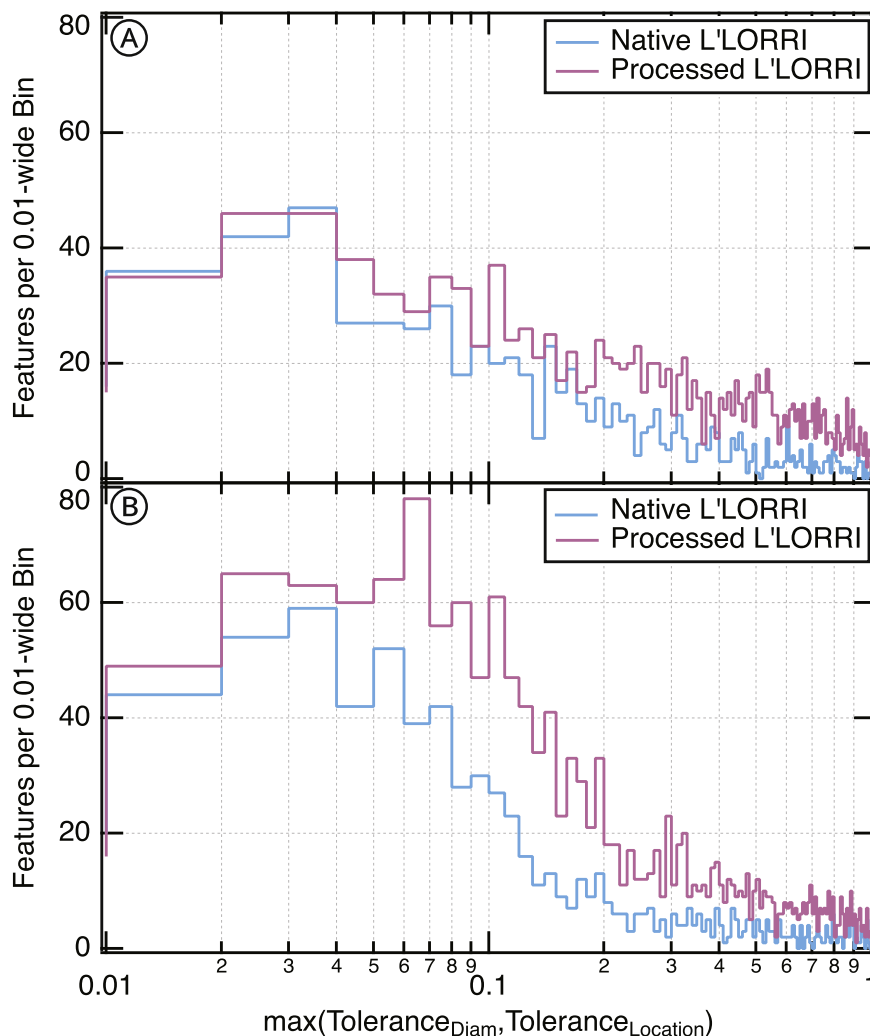


Figure 3. Crater match tolerance between L'LORRI and ground-truth craters. The horizontal axis is the maximum of the two cluster parameters used to match craters between the catalogs, since these parameters were varied (see main text). In automatic matching of craters between the different catalogs, clustering parameters were very small to begin with and then increased in order to match the best-matching features first. (A) Results from circle-based fits, and (B) results for ellipse-based fits to crater rims. These show that more features were found with the processed images than native (that curve is higher in both graphs), that more features are matched with tighter tolerances in all cases, and that more features were matched with tighter tolerances when using ellipse-fit minor axes than circle-fit diameters (i.e., there is better agreement between ellipse minor axes and ground-truth diameters).

modified version includes two reachability parameters, one based on crater location scaled by diameter and the other based on the similarity of the diameters. For this work, to ensure the best matches were made first, we used a sliding scale of reachability, from 0.001 for both parameters up to 1.0. By 1.0, the crater diameters could be up to 50% different, and locations offset by a full crater diameter, which is extremely generous for this exercise. Figure 3 shows a graph of reachability versus number of craters matched using circle and ellipse fits, illustrating that the majority of features are matched with very small reachability tolerances. If reachability were further restricted, the number of FNs would increase; the reverse is also true.

The second analysis was conducted for the entire mapped region as well as longitude bands to try to determine if there was any dependence with solar incidence. Longitude bands are a reasonable proxy for solar incidence due to the Moon's inclination and topography: the terminator was at approximately 10.1°E for the northernmost regions and 10.8°E for the southernmost regions during imaging, which was linear enough that longitude scales with solar incidence almost independent

of latitude for our region of interest. Due to the significant topographic shading near the terminator, we selected longitude bands that were 10° wide and then contracted to $\approx 5^{\circ}$ wide: $25^{\circ}\text{--}15^{\circ}\text{W}$ ($i \approx 55^{\circ}\text{--}65^{\circ}$), $15^{\circ}\text{--}5^{\circ}\text{W}$ ($i \approx 65^{\circ}\text{--}75^{\circ}$), $\pm 5^{\circ}\text{E}$ ($i \approx 75^{\circ}\text{--}85^{\circ}$), and $5\text{--}8.7^{\circ}\text{E}$ ($i \approx 85^{\circ}\text{--}89^{\circ}$).

We found that smaller craters appear elongated in the L'LORRI images, which is consistent with the intrinsic shape of the PSF (Weaver et al. 2023). Since S.J.R.'s crater identification method automatically includes both circle and ellipse fits, we performed the above two analyses twice, once using crater diameters from circle fits and once using minor axes from ellipse fits.

Finally, to make comparisons between the numerous graphs and different data sets easier to follow, we have used the following color scheme in our graphs: For analysis 1 (SFD), the ground-truth data are yellow, native L'LORRI data lighter blue, and processed L'LORRI data pink; for analysis 2 (crater-crater comparisons), TPs are green, FPs are blue, and FNs are red, while native L'LORRI data are darker shades and processed L'LORRI are lighter shades.

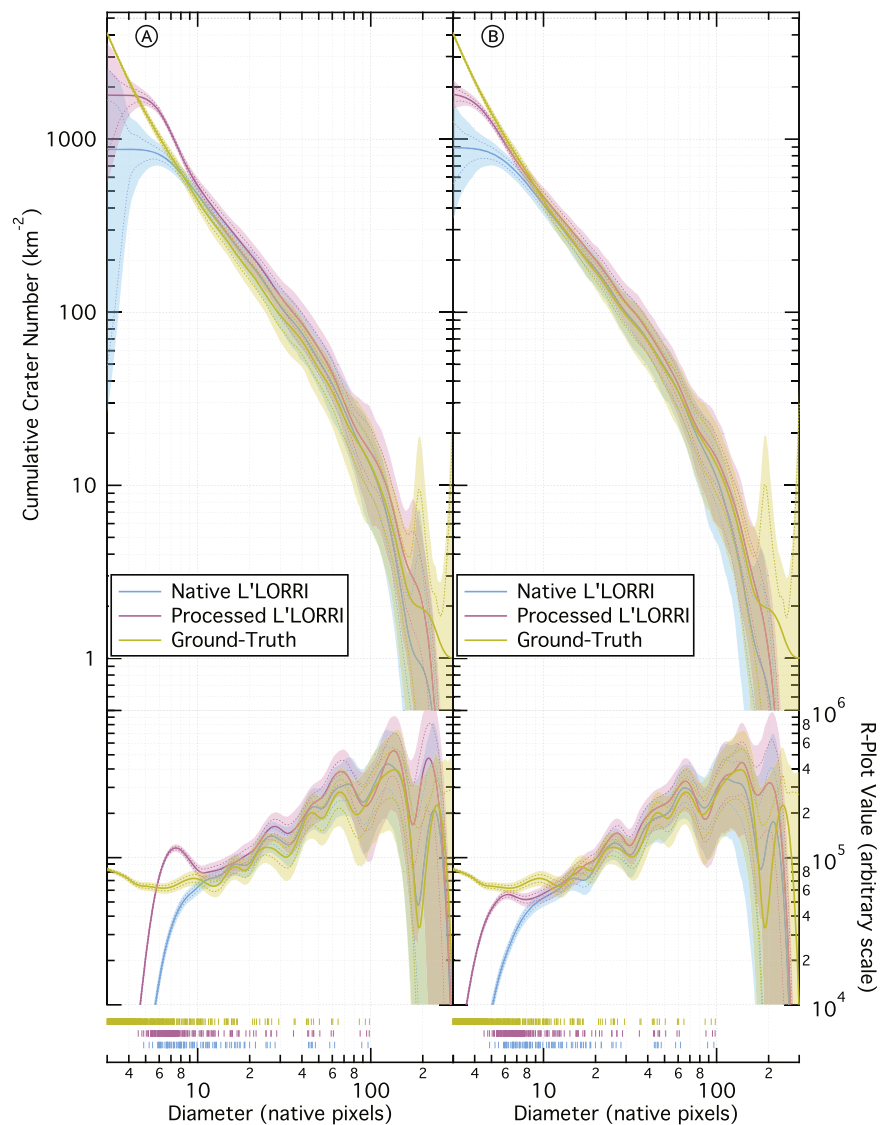


Figure 4. SFD_{EDF} analysis for craters mapped on L'LORRI images compared with the ground-truth database. The SFD_{EDF} s were constructed using Gaussian kernels with $0.1 \cdot D$ widths, and the bootstrap with replacement method was run 10,000 times for each data set to produce the confidence envelopes. Rug plots on the bottom show original crater diameters that were used to construct each SFD_{EDF} . Shaded confidence bands are 95% and dotted are 1σ (68%). Panel (A) shows diameters from circle fits, while panel (B) shows minor axes from ellipse fits.

5. Results

In this section, all results have been scaled to native L'LORRI pixels unless otherwise stated, which in this test had a ground scale of ≈ 1.25 km.

5.1. Size–Frequency Distribution Analysis

The SFD analysis is shown in Figure 4 (and the Appendix) for both diameters from circle fits and the minor axes from ellipse fits as $CSFD_{EDF}$ and $RSFD_{EDF}$ plots. As one would expect, the crater populations from both image sets match well at large diameters regardless of plot type and regardless of using native or processed L'LORRI images. They begin to diverge at ≈ 10 pix in a complex way.

For the $RSFD$ circle-based fits, there is a very distinct falloff of craters identifiable in native images for $\lesssim 10$ pix. Due to the cumulative nature of a $CSFD$, the deviation from ground-truth appears at $\lesssim 8.5$ pix, slightly masking the failure to identify slightly larger craters. The deviation for craters identified on

processed images is also $\lesssim 10$ native pixels ($\lesssim 20$ processed pixels), but instead of a decrease it is a marked increase.

To investigate this phenomenon, we visually examined the images and specifically looked at small craters. Samples are shown in Figure 5. We found that the L'LORRI camera appears to spread small craters out into ellipses, consistent with the extended, bimodal L'LORRI PSF (Weaver et al. 2023). The PSF is large and distorted enough that it affects craters at a native scale of $\lesssim 10$ pix; the further processing enhances the visibility of small craters, but those small craters are more affected by the PSF relative to their overall size, making circle-fit diameters appear to be larger than the ground truth.

To test this explanation, we used the minor axes from the ellipse fits of the crater rims. The minor axes in lieu of crater diameters appear to give better overall matches with tighter tolerances to the ground-truth database (Figure 3). Examining the SFD (Figure 4), the results are mixed. Looking at the $CSFD_{EDF}$, the native L'LORRI curve diverges by $>1\sigma$ for craters $\lesssim 8.0$ pix, similar to the circle diameter analysis. For the

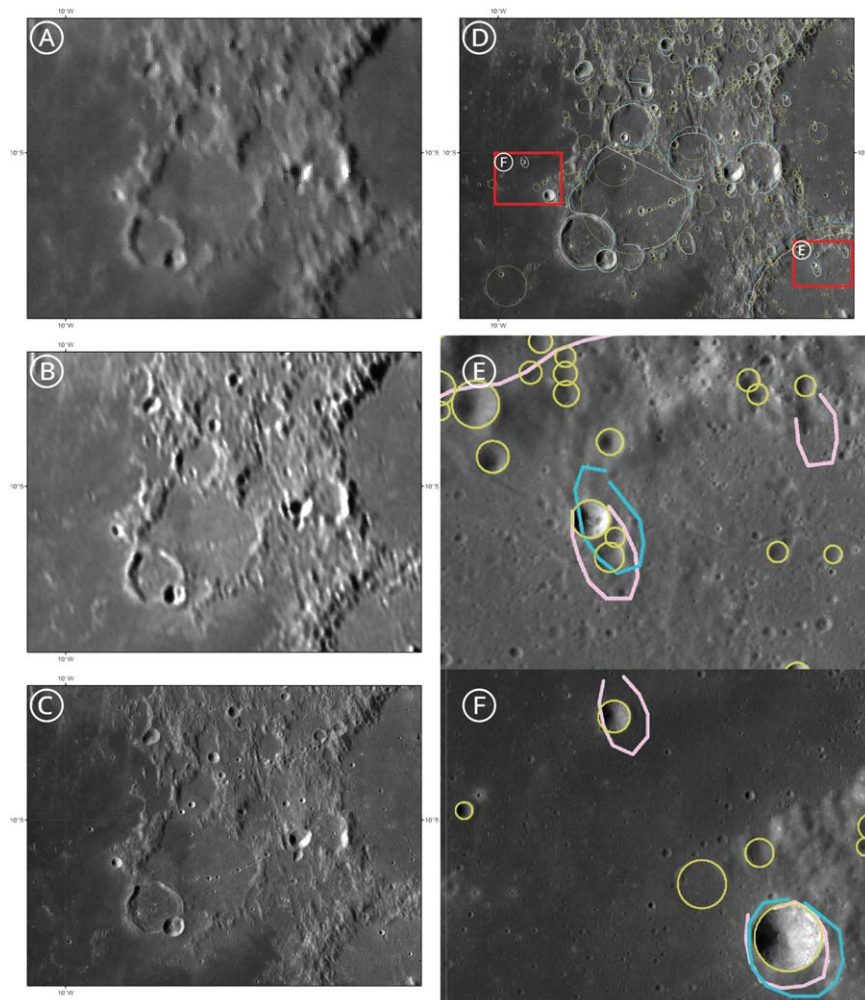


Figure 5. Sample region of the Moon showing different imaging and crater identifications from that imaging. (A) L'LORRI native image. (B) L'LORRI processed image. (C) LROC-WAC mosaic. The lighting geometry was approximately the same in the LROC-WAC as in the Lucy L'LORRI for this region. The panels on the right use the same color-coding as the rest of this work, where yellow are ground-truth craters, cyan are native L'LORRI, and pink are processed L'LORRI. (D) Crater identifications in each of the three data sets. (E) and (F) are close-ups of regions from (D) showing idealized circles from the ground-based database and actual rim outlines traced from the two L'LORRI data sets (while it appears as though there is large vertex spacing, the spacing is ≈ 1.5 km, which is ≈ 1 native L'LORRI pixel).

processed data, the divergence is $\lesssim 5.5$ pix and there is no apparent broadening effect to larger diameters. However, the $RSFD_{EDF}$ tells a more accurate story since the CSFD will mask diameter-specific behavior. The $>1\sigma$ deviation based on the native data is $\lesssim 11$ pix, and the deviation for craters on the processed image data is also $\lesssim 11$ pix.

We suspect that there are several issues that lead to this result. First, the diameter-based results for the native images were also broadened, but to a much lesser degree, which buoyed the $RSFD$ at slightly larger diameters to make it appear to agree with the ground-truth data more. Second, the absence or significant reduction of that broadening in both ellipse data sets shows that, while there is a deficit of craters in the ~ 6 – 11 pix range from the processed images, craters *are* being detected and so boost the $RSFD$ relative to craters from the native image until the falloff from incompleteness dominates; the end result is to approximately match the SFD shape for $\gtrsim 7$ pix. This scenario is presented in Figure 6.

As a further test of the diameter broadening, we used the crater-to-crater matching and examined the ratio of diameters found with Lucy images versus those in the ground-truth database. Figure 7 illustrates the results for diameters and

minor axes; there would be a straight, horizontal line at 1.0 if the Lucy-based diameters matched the ground-truth crater diameters at all sizes. Instead, the larger values on the vertical axis at smaller values on the horizontal axis show that smaller-diameter craters appear larger in L'LORRI than they do in LROC-WAC. This effect is more pronounced at larger sizes for diameters based on circle fits than it is for minor axes based on ellipse fits. Additionally, the power-law fit from the minor axes comparison indicates that the minor axes will underestimate crater size by $\sim 5\%$ for larger crater diameters, though there is significant scatter.

In summary, the results described in this section demonstrate that one can derive what is likely a complete SFD for craters $\gtrsim 10$ – 11 pix, and the results are within 1σ uncertainties regardless of using crater diameters or ellipses, or when using native L'LORRI or processed L'LORRI images. Further discussion is given in later sections.

5.2. Crater-to-crater Analysis

One potential concern about the L'LORRI processing is that it will create artificial craters via ringing effects from the deconvolution. This might not show up in the SFD-based

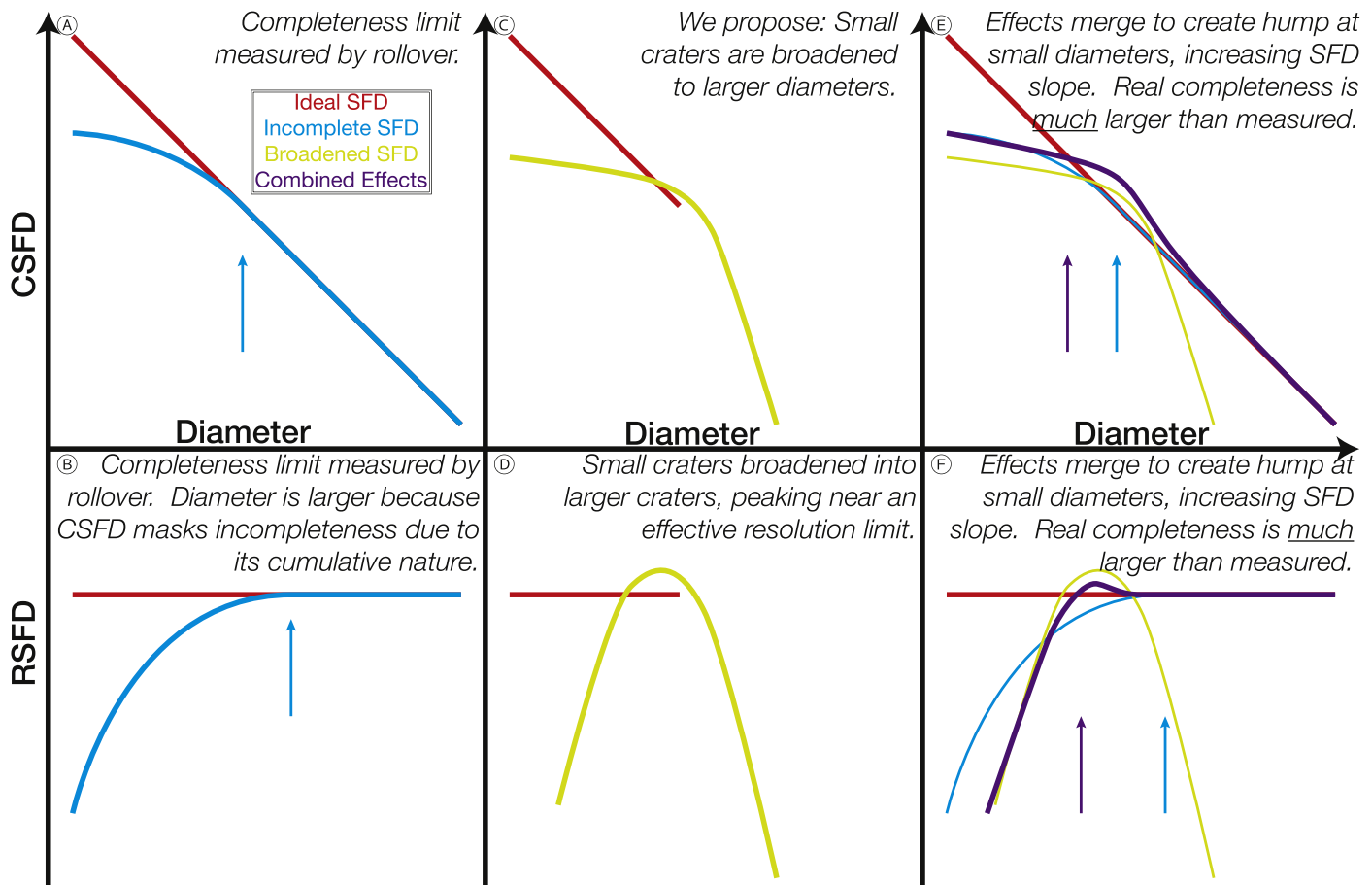


Figure 6. Model illustrating our proposed explanation for the Lucy-based SFDs, specifically explaining the artifact in circle-fit crater diameters from “processed” L’LORRI images near $\approx 6\text{--}10$ pix. Top shows cumulative, bottom shows relative plots; in all panels, the red line is an idealized $dN/dD \propto D^{-3}$ function. In the left panel, an incomplete SFD is shown in the cyan curve, and the completeness based on the observed rollover is marked; it is at a false, smaller diameter on the CSFD because the CSFD masks diameter-specific behavior due to its cumulative nature. In the middle column, the small-crater SFD is measured to be broadened based on a combination of various factors, but in our scenario the broadening is dominated by the PSF. Depending on the severity of the broadening, the yellow curve may or may not be above the red; here, it is shown to be above the red because we think that is what is happening at $\sim 6\text{--}10$ pix for circle-fit craters. In the right panels, the effects are convolved in the purple curve, resulting in the hump observed at small craters and then fall off to observed incompleteness. In reality, completeness is at a larger diameter, but the broadening of small craters artificially inflates the SFD, making it appear as though completeness is at a false, smaller diameter.

analysis because “cratering by deconvolving” might produce an SFD that mimics the real crater SFD, but those false craters would not correspond to geologically real features. To investigate this possible phenomenon, the cluster analysis was run to match craters derived from L’LORRI images against the ground-truth database. For this analysis, the region was examined en masse and also in longitude bins that are analogous to solar incidence bins.

Figure 8 is primarily used to interpret this crater-crater comparison analysis, and the results are shown in this figure independent of incidence angle. The TP rate (TPR), real craters that were identified divided by all real craters, is $>80\%$ for diameters from circle fits for craters >16 pix from native L’LORRI; the TPR is $>80\%$ for craters >8 pix from processed L’LORRI images. Reaching the 80% threshold is, therefore, accomplished for craters a factor of 2 smaller from the processed images (though whether those diameters are accurate or not is subject to the analysis from Figure 7, discussed in the previous section and the final section). For ellipse-based fits’ minor axes, the rate is $>80\%$ for >16 pix and >11 pix, respectively, an improvement in diameter by $\sqrt{2}$ at this 80% threshold. The rates drop below 50% TPR for craters >6 pix and >4 pix for circle and ellipse fits, also an improvement of

$\sqrt{2}$. The false-negative rate (those real craters in the ground-truth database not detected in the L’LORRI images) is $1 - \text{TPR}$.

The fraction of FPs, L’LORRI-detected features that are not in the ground-based database, is the most indicative of the concern about cratering by deconvolution. Fortunately, FPs are fairly stable across all diameter ranges at $\lesssim 10\%$, and they do not vary significantly between the native L’LORRI images and the processed L’LORRI images. This invariance between the native and processed L’LORRI is interpreted as evidence against the cratering by deconvolution concern. When we include lower-confidence features from the Robbins (2019) database, the FP rate dropped further. The spike in the 128 pix bin (Figure 8) is due to a single feature and is not indicative of a significant mismatch.

While this analysis is important to provide an overall understanding of the rates across the region of interest, we can also examine whether the results change as a function of solar incidence angle. The ground-truth database was constructed from a wide array of data sets, and the image-based data had generally consistent $\sim 70^\circ$ solar incidence angles throughout. The Lucy lunar imaging did not. Figure 9 shows the results in rows as a function of solar incidence angle, where the purpose is to determine if the results vary as a function of solar

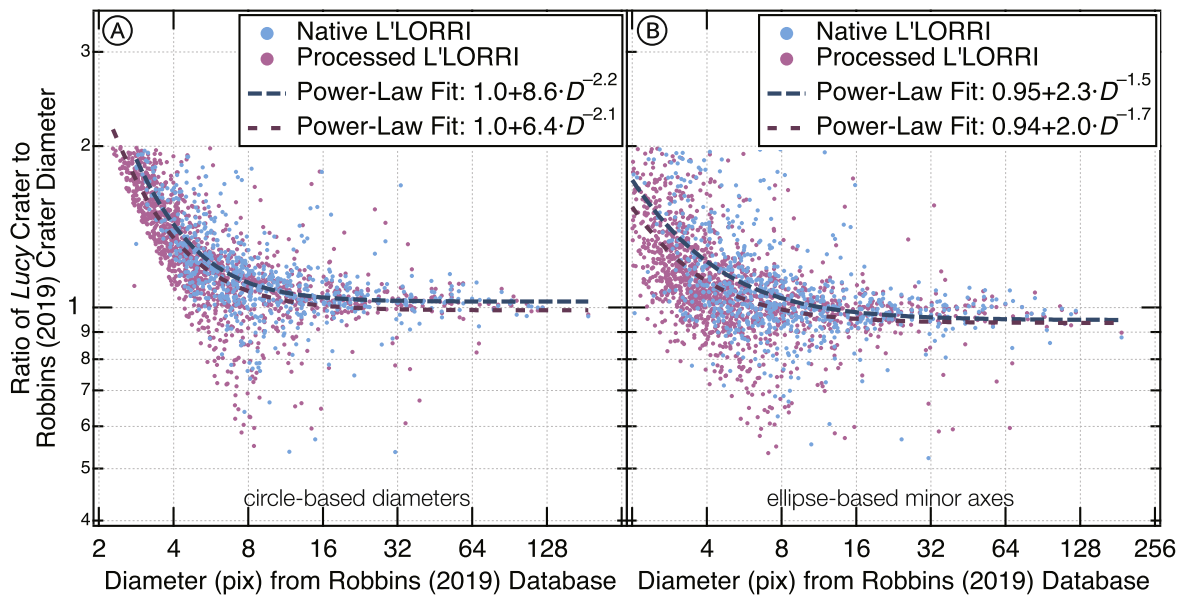


Figure 7. Ratio of crater size as a function of crater diameter in the ground-truth database for (A) diameters based on circle fits, and (B) minor axes of ellipse fits. A horizontal line of 1.0 would mean that the crater sizes from L'LORRI are identical to those from the ground-truth database for all diameters. Sharp cutoffs (diagonal in panel (A) and no data >2) are due to cutoffs in matching craters. Power-laws were fit to each data distribution using an orthogonal distance regression method, and parameters are given in the figure legends.

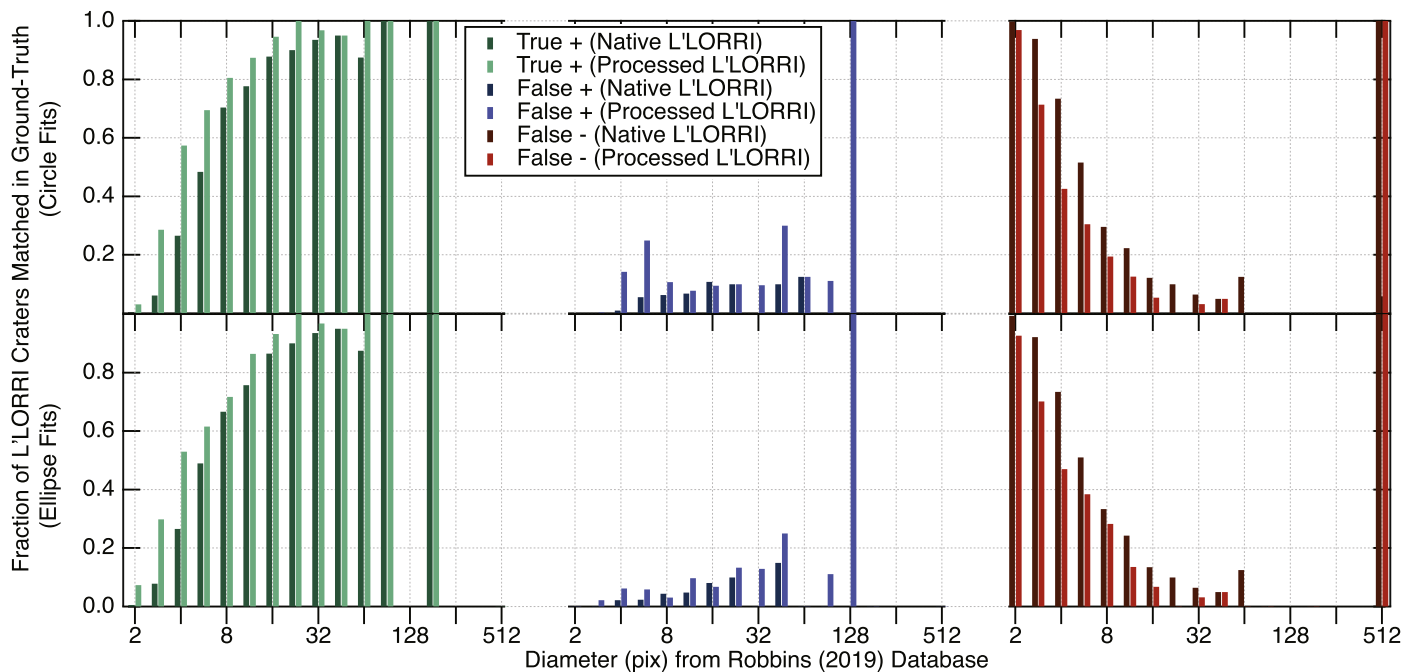


Figure 8. True positives (left), false positives (middle), and false negatives (right) for features detected on L'LORRI images with circle-fit diameters (top) or ellipse-fit minor axes (bottom), with color brightness indicating whether those features were identified on native L'LORRI or processed L'LORRI images. The data are binned such that bin b_i contains data from diameters $(D_{i-1}, D_i]$, and the bars straddle the bin value b_i . In this analysis, if a feature was matched to the Robbins (2019) database, then the diameter used for the horizontal axis value is the crater diameter from the Robbins (2019) database and *not* the size found using L'LORRI images.

illumination. The first-order result is that, in general, crater detection suffers when $i \lesssim 65^\circ$, which is evidenced by TP rates in the top row for larger crater diameters not being as high ($\sim 100\%$) as for other incidence angles. Additionally, across all incidence-angle ranges, craters identified on the processed images have TP rates larger than those identified on native L'LORRI images. Unfortunately, the FP rate with $i \lesssim 75^\circ$ from the processed L'LORRI images tends to be significantly higher than the FP on native L'LORRI images (compare the blue bars in the first versus second columns, e.g., for circles in the

$i = 65^\circ - 75^\circ$ second row, for craters 4–16 pix, the fraction of FP is 12% on native images versus 33% on processed). This result indicates that there *does* appear to be a cratering by deconvolution effect, though the magnitude of the effect may depend on incidence angle. If this were not a cratering by deconvolution effect, then we would see comparable FPs in both image data sets. Cratering by deconvolution is not as apparent in Figure 8 because there were many more craters found at high solar incidence.

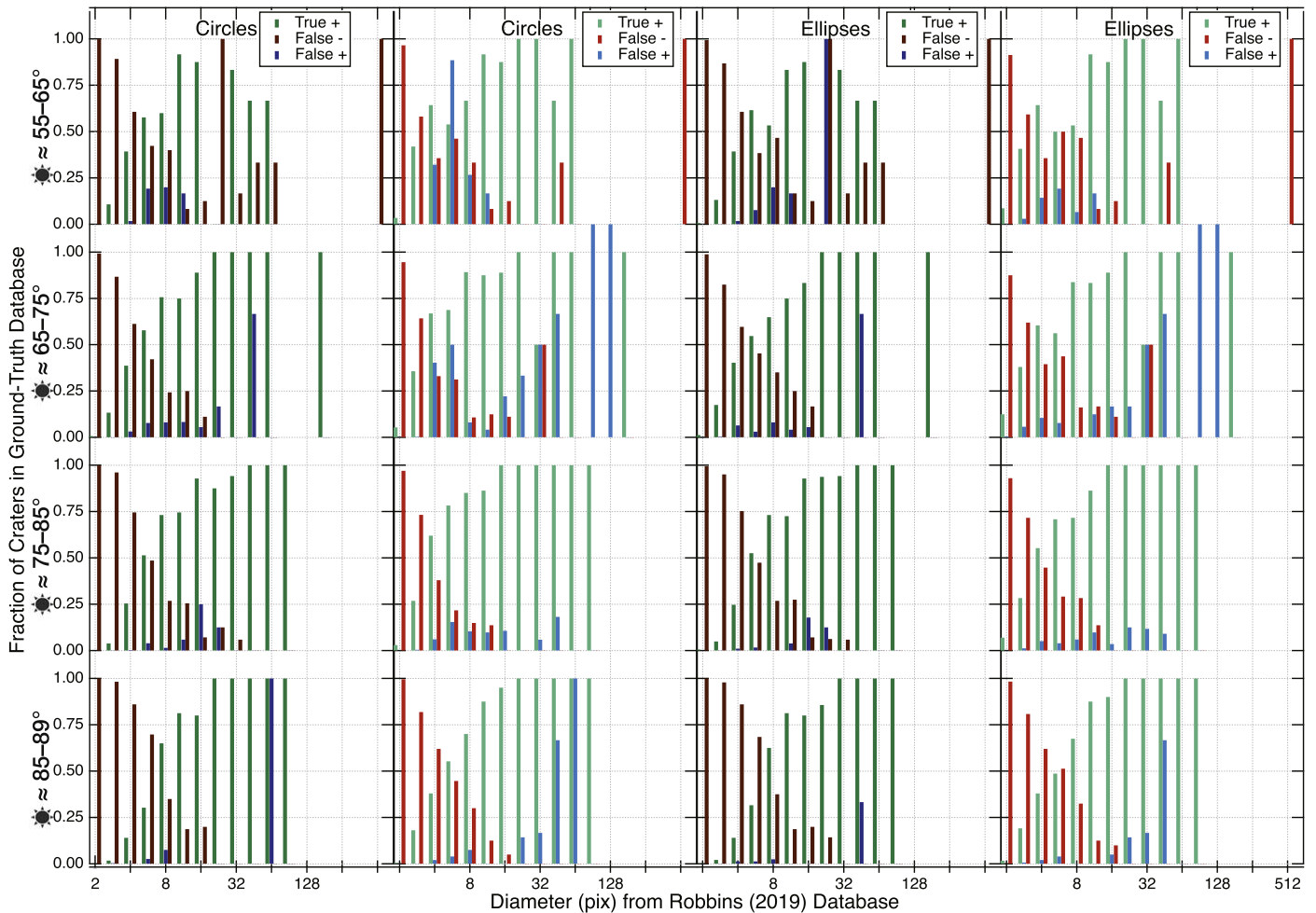


Figure 9. Similar to Figure 8, including the method of data binning. In this version, the TP, FN, and FP have been interleaved, but they still remain separated by native L'LORRI (first and third columns) or processed L'LORRI (second and fourth columns), and they are separated by circle-fit diameters (first two columns) and ellipse-fit minor axes (last two columns). In this version, rows indicate solar incidence range, where the top row covers lighting during the Lucy encounter of $i \approx 55^\circ\text{--}65^\circ$, up to $i \approx 85^\circ\text{--}89^\circ$ in the bottom row. The purpose of this figure is to determine if and how the TP, FN, and FP rates vary based on Sun angle.

6. Synthesis and Discussion

This study set out to answer the question of whether creating a deconvolved, well-sampled (at least Nyquist-sampled, or >2 pix across the PSF) image from planetary data could decrease the minimum diameter to which craters can be reliably detected and measured, and to determine how well images from L'LORRI can be used to produce a crater population in general. This test was performed for Lucy's L'LORRI image data of Earth's Moon, representing the only chance in the mission to compare a Lucy-detected crater population with a crater database constructed from significantly better, independent data from NASA and other space-agency assets. Results were analyzed using primarily two different methods.

One complicating factor in this analysis is that the L'LORRI PSF is bimodal, approximately represented by an ellipsoid, which is oversampled by the L'LORRI camera. Indications that this could present a factor for data interpretation came from examination of small craters on the images themselves, where craters $\lesssim 10$ pix across were noticeably elongated (e.g., Figure 5). In an attempt to mitigate this issue, or better understand its effects, the analyses were conducted for both crater diameters from circle fits to the rim traces and for minor axes from ellipse fits to those same rim traces.

Results from the SFD analysis using circle fits indicated reliable crater statistics could be gathered for craters $\gtrsim 10$ pix, while results for ellipse-based fits were slightly worse at $\gtrsim 11$ pix. Our proposed scenario of crater completeness and broadening (Figure 6) suggests that the real completeness might be a few pixels larger than these minima. The primary difference between the circle and ellipse SFDs was that the circle-based diameters show a very strong broadening effect to larger diameters due to the PSF, supported by the analysis in Figure 7, which mimics the lunar SFD. When using the minor axes of ellipse fits, crater sizes are reproduced more faithfully relative to ground truth, but broadening is still an issue for craters several pixels across, and larger crater diameters are suppressed by a few percent. We conclude from this that both crater diameters and ellipse minor axes will be useful for Lucy crater measurement, where ellipses can be more informative for smaller craters and diameters for larger. The exact transition will depend on the application, but, based on Figure 7, it is probably ≈ 15 native pixels when emission angles are near 0° . It should be noted that the Lucy encounters are currently being designed under the assumption that features ≥ 5 "resolution elements" can be resolved and accurately measured, where 1 "resolution element" = 3 native L'LORRI pixels. Ergo, this

conservative cutoff in mission planning to meet Lucy’s primary science goals aligns well with reliability results from this study.

While the SFD is indicative of the overall population, it is more informative to look at the crater-to-crater matched results from Section 5.2 because of the broadening from smaller to larger diameters. The incidence-angle-independent analysis suggests that Lucy imaging should be able to detect $\gtrsim 80\%$ of impact craters $\gtrsim 11$ pix; however, based on Figure 7, we will be unable to accurately measure the diameters of those ~ 11 pix diameter craters. We found that the circle versus ellipse fits do not change this detectability analysis in any significant way, though more craters were matched more accurately to the ground-truth database when using the minor axes rather than diameters (Figure 3). Regardless, we also found that the processing of L’LORRI images tended to improve recovery of the ground-truth craters by up to $2\times$ for craters with diameters ~ 4 pix and improve them by $\sim +10\%$ for craters with real diameters ~ 8 – 25 pix. This has the effect of getting the same detectability rate for native L’LORRI images but down by approximately one $\sqrt{2}$ diameter bin. However, it again must be emphasized that, while we have improved detectability, we have not improved crater measurement accuracy on the processed images, and so while we can see more small craters and we might derive SFDs that match an expected production function to ~ 11 pix, it is likely that we will have only accurately measured features as small as ≈ 15 pix across.

The above paragraph results are independent of solar incidence angle. As one would expect given past work (Wilcox 2005; Ostrach et al. 2011; Richardson et al. 2022) and general knowledge in the geologic community, the detectability of craters fell off significantly for Sun angles $\lesssim 65^\circ$. Given the nature of flyby missions, this could significantly affect the surface area over which Lucy can provide reliable impact crater statistics. Additionally, for incidence angles $\lesssim 75^\circ$, the results indicate that the FP rate of detection was nearly 50% in some diameter bins based on the processed images, but less than half this rate based on native images. This raises the cautionary issue of whether we will face “cratering by deconvolution,” where the ringing effect endemic to deconvolution might produce FPs in areas of images with higher Sun. This is partially mitigated by the observation that reliable recovery ($>80\%$) can be done for the $i = 65^\circ$ – 75° range for craters $\gtrsim 16$ pixels across. A possible complicating factor is that the

lunar terrain observed by L’LORRI was approximately all maria for $i < 75^\circ$, and the observed terrain was approximately all highlands for $i > 75^\circ$. Whether the terrain type affects recoverability of real features could not be studied in this test and remains an open question.

The results of this work and analyses indicate that reliable impact crater statistics and measurements should be recoverable for Lucy targets within the ≥ 5 resolution elements (≥ 15 native pixels) encounter planning. However, at smaller incidence angles, caution will be needed in interpreting features in the processed images to try to mitigate processing artifacts from being interpreted as impact craters. Further, any attempts to analyze craters < 5 resolution elements will need to be met with significant caution, where their diameters will likely appear larger than they really are, and their detectability will diminish sharply $\lesssim 3$ – 4 resolution elements (10–11 native L’LORRI pixels) even under favorable lighting and viewing geometries. Additional viewing geometry effects, such as emission angle, will also need to be evaluated as the mission progresses, since this lunar imaging test did not study them. While this work was specifically done in support of the Lucy mission, the basic findings should be applicable to other spacecraft flybys, though it will vary based on each camera’s optics and, specifically, their PSFs.

Acknowledgments

The authors acknowledge funding from NASA’s Lucy mission. The authors acknowledge two anonymous reviewers whose feedback improved this work.

Appendix

For those who prefer interpreting the more classic unbinned cumulative and binned relative SFDs (Arvidson et al. 1978), we include two additional figures in this Appendix as alternatives to Figure 4. The first, Figure 10, shows 1978-only versions; Figure 11 shows both versions on top of each other and demonstrates that they agree well. The CSFDs are a basic histogram, while the RSFDs in the bottom panels are binned in $2^{1/8}$ multiplicative bins (finer fidelity than $2^{1/2}$). Error bars are Poisson-based $N^{1/2}$. As can be seen, the displays—and interpretations—are the same regardless of graphing technique.

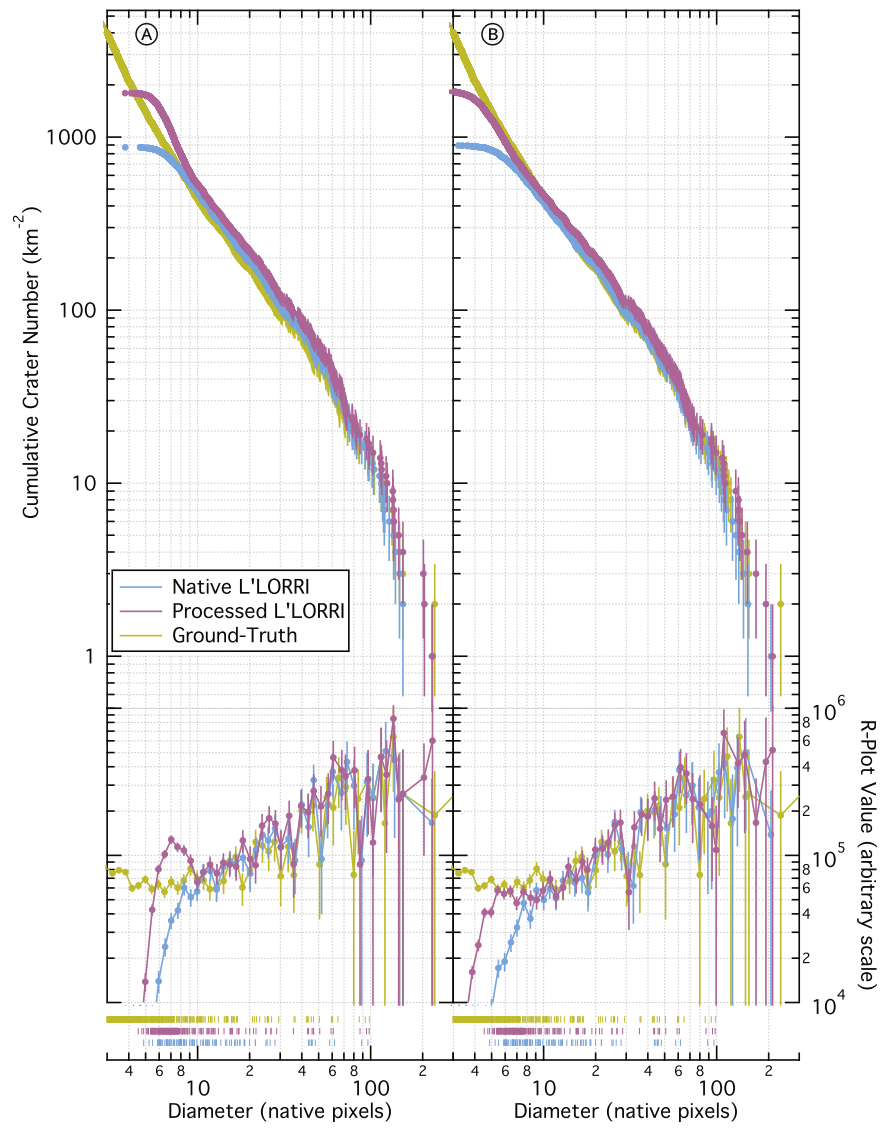


Figure 10. Same as Figure 4, but uses the more classic binned method of the Arvidson et al. (1978) for the relative form (bottom) and unbinned for the cumulative form (top). In the relative version, lines connecting the points have been drawn.

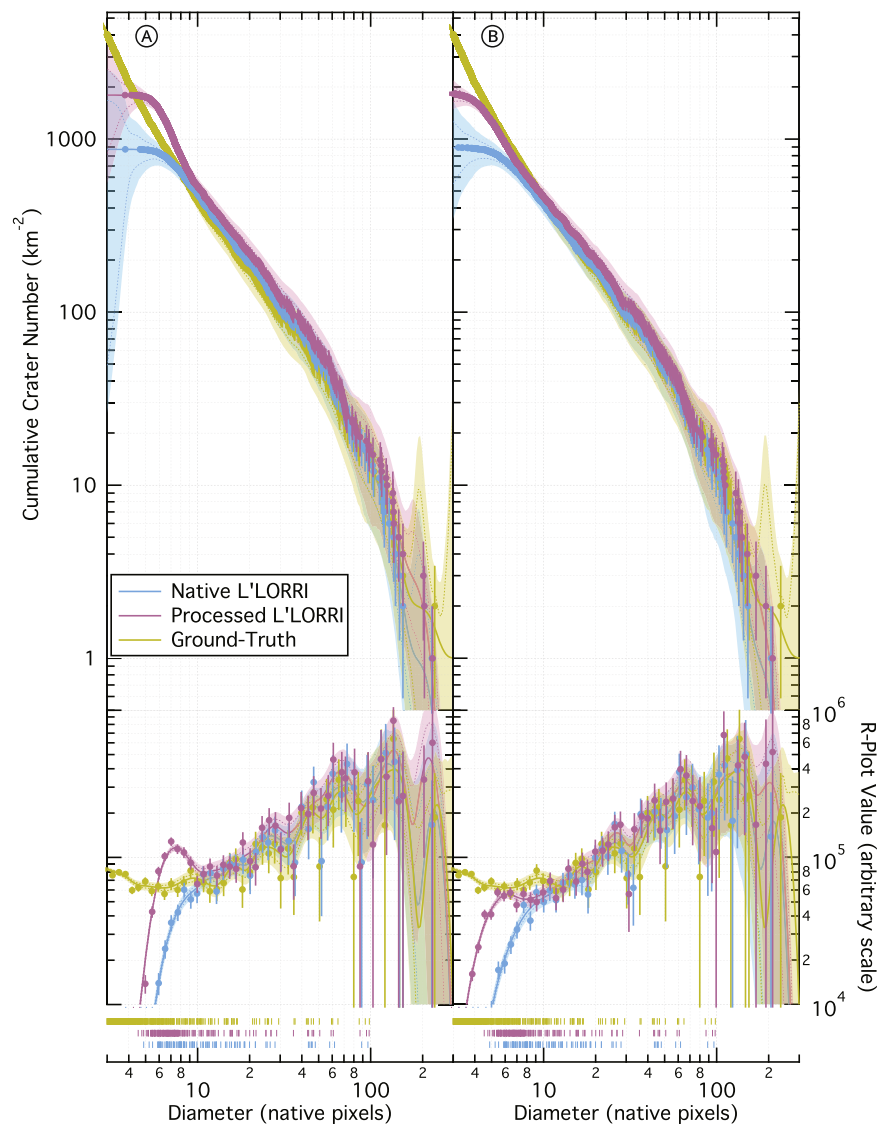


Figure 11. Figures 4 and 10 stacked, with connecting lines in the RSFD removed. This figure demonstrates that the graphing method neither alters the results nor the interpretation.

ORCID iDs

Stuart J. Robbins <https://orcid.org/0000-0002-8585-2549>
 Olivier Barnouin <https://orcid.org/0000-0002-3578-7750>
 Tod R. Lauer <https://orcid.org/0000-0003-3234-7247>
 John Spencer <https://orcid.org/0000-0003-4452-8109>
 Simone Marchi <https://orcid.org/0000-0003-2548-3291>
 Harold A. Weaver <https://orcid.org/0000-0003-0951-7762>
 Stefano Mottola <https://orcid.org/0000-0002-0457-3872>
 Hal Levison <https://orcid.org/0000-0001-5847-8099>
 Neil Dello Russo <https://orcid.org/0000-0002-8379-7304>

References

- Arvidson, R., Boyce, J., Chapman, C., et al. 1978, Standard techniques for presentation and analysis of crater size-frequency data *NASA TM 79730*, NASA <https://ntrs.nasa.gov/api/citations/19780014063/downloads/19780014063.pdf>
- Ester, M., Kriegel, H.-P., Sander, J., & Xu, X. 1996, in *Second Int. Conf. on Knowledge Discovery and Data Mining (KDD'96)*, ed. E. Simoudis, J. Han, & U. Fayyad (Washington, DC: AAAI Press), 226
- Lauer, T. R. 1999, *PASP*, 111, 227
- Levison, H. F., Olkin, C. B., Noll, K. S., et al. 2021, *PSJ*, 2, 171
- Lindler, D. J., A'Hearn, M. F., Besse, S., et al. 2013, *Icar*, 222, 571
- Lucy, L. B. 1974, *AJ*, 79, 745
- Marchi, S., Bell, J. F., Bierhaus, B., & Spencer, J. 2023, *SSRv*, 219, 44
- Ostrach, L. R., Robinson, M. S., Denevi, B. W., & Thomas, P. C. 2011, *LPSC*, 42, 1202
- Richardson, M., Plazas Malagón, A. A., Lebofsky, L. A., et al. 2022, *OJAp*, 5, 2
- Richardson, W. H. 1972, *JOSA*, 62, 55
- Robbins, S. J. 2019, *JGRE*, 124, 871
- Robbins, S. J., Antonenko, I., Kirchoff, M. R., et al. 2014, *Icar*, 234, 109
- Robbins, S. J., Riggs, J. D., Weaver, B. P., et al. 2018, *M&PS*, 53, 891
- Robbins, S. J., Singer, K. N., Bray, V. J., et al. 2017, *Icar*, 287, 187
- Robinson, M. S., Brylow, S. M., Tschimmel, M., et al. 2010, *SSRv*, 150, 81
- Schenk, P. M., Beyer, R. A., McKinnon, W. B., et al. 2018a, *Icar*, 315, 124
- Schenk, P. M., Beyer, R. A., McKinnon, W. B., et al. 2018b, *Icar*, 314, 400
- Szpak, Z. L., Chojnacki, W., & van den Hengel, A. 2015, *J. Math Imaging Vis*, 52, 173
- Weaver, H. A., Wilson, J. P., Conrad, S. J., et al. 2023, *SSRv*, 219, 82
- Wilcox, B. B., Robinson, M. S., Thomas, P. C., & Hawke, B. R. 2005, *M&PS*, 40, 695